

Fast Outflows Identified in Early Star-Forming Galaxies at $z = 5-6$

YUMA SUGAHARA,^{1,2} MASAMI OUCHI,^{1,3} YUICHI HARIKANE,^{1,2,4} NICOLAS BOUCHÉ,⁵ PETER D. MITCHELL,⁶ AND JÉRÉMY BLAIZOT⁵

¹*Institute for Cosmic Ray Research, The University of Tokyo, 5-1-5 Kashiwanoha, Kashiwa, Chiba 277-8582, Japan*

²*Department of Physics, Graduate School of Science, The University of Tokyo, 7-3-1 Hongo, Bunkyo, Tokyo, 113-0033, Japan*

³*Kavli Institute for the Physics and Mathematics of the Universe (WPI), University of Tokyo, Kashiwa 277-8583, Japan*

⁴*National Astronomical Observatory of Japan, 2-21-1, Osawa, Mitaka, Tokyo 181-8588, Japan*

⁵*Univ Lyon, Univ Lyon1, Ens de Lyon, CNRS, Centre de Recherche Astrophysique de Lyon UMR5574, F-69230 Saint-Genis-Laval, France*

⁶*Leiden Observatory, Leiden University, PO Box 9513, NL-2300 RA Leiden, the Netherlands*

ABSTRACT

We present velocities of galactic outflows in seven star-forming galaxies at $z = 5-6$ with stellar masses of $M_* \sim 10^{10.1} M_\odot$. Although it is challenging to observationally determine the outflow velocities, we overcome this by using ALMA [C II]158 μm emission lines for systemic velocities and deep Keck spectra with metal absorption lines for velocity profiles available to date. We construct a composite Keck spectrum of the galaxies at $z = 5-6$ with the [C II]-systemic velocities, and fit outflow-line profiles to the Si II $\lambda 1260$, C II $\lambda 1335$, and Si IV $\lambda \lambda 1394, 1403$ absorption lines in the composite spectrum. We measure the maximum (90%) and central outflow velocities to be $v_{\text{max}} = 700_{-110}^{+180} \text{ km s}^{-1}$ and $v_{\text{out}} = 400_{-150}^{+100} \text{ km s}^{-1}$ on average, respectively, showing no significant differences between the outflow velocities derived with the low to high-ionization absorption lines. For $M_* \sim 10^{10.1} M_\odot$, we find that the v_{max} value of our $z = 5-6$ galaxies is 3 times higher than those of $z \sim 0$ galaxies and comparable to $z \sim 2$ galaxies. Estimating the halo circular velocity v_{cir} from the stellar masses and the abundance matching results, we investigate a $v_{\text{max}}-v_{\text{cir}}$ relation. Interestingly, v_{max} for galaxies with $M_* = 10^{10.0-10.8} M_\odot$ shows a clear positive correlation with v_{cir} and/or the galaxy star formation rate over $z = 0-6$ with a small scatter of $\simeq \pm 0.1$ dex, which is in good agreement with theoretical predictions. This positive correlation suggests that the outflow velocity is physically related to the halo circular velocity, and that the redshift evolution of v_{max} at fixed M_* is explained by the increase in v_{cir} toward high redshift.

Keywords: galaxies: formation — galaxies: evolution — galaxies: ISM — galaxies: kinematics and dynamics

1. INTRODUCTION

The energy and momentum inputs from supernovae (SNe) and active galactic nuclei (AGNs) accelerate the inter-stellar medium (ISM) outwards, and launch galactic-scale outflows. The outflows are composed of the various ISM phases from cold molecular to hot gas (e.g., Veilleux et al. 2005). AGN-driven outflows are thought to play an important role to quench the star-forming activity in massive galaxies, and recent observational work reports the evidence that the AGN feedback may also operate in low-mass galaxies (Penny et al. 2018; Manzano-King et al. 2019). On the other hand, SN-driven outflows are thought to affect galaxies primarily in low-mass regime. The mass, momentum, energy, and metal budgets of the outflows leaked from the star-forming galaxies are theoretically important for regulating the star-forming activity in low-mass galaxies, creating the mass-metallicity relation of galaxies, and polluting the circumgalactic medium and intergalactic medium (IGM) (for a re-

view, see Somerville & Davé 2015; Dayal & Ferrara 2018). Thus, the outflows in star-forming galaxies driven by SNe have a large impact on the galaxy and IGM evolution. Many theoretical studies contribute to revealing the details of the outflow properties using cosmological (zoom-in) simulations (Oppenheimer et al. 2010; Muratov et al. 2015; Christensen et al. 2016; Ceverino et al. 2016; Mitchell et al. 2018; Nelson et al. 2019).

In the rest-frame far-ultraviolet (FUV; 1000–2000 Å) to optical bands, metal absorption and emission lines are useful to trace the kinematics of the cold and warm outflowing gas. The outflow velocity along the line of sight is estimated with the “down-the-barrel” technique, which measures blueshifts of the absorption lines in the galaxy spectra (e.g., Heckman et al. 2000; Martin 2005; Rupke et al. 2005a,b; Steidel et al. 2010; Martin et al. 2012; Zhu et al. 2015; Heckman et al. 2015; Chisholm et al. 2015, 2016a, 2017; Roberts-Borsani & Saintonge 2019; Concas et al. 2019), while the outflowing gas far from the galaxy is detected with the absorption lines in the background-quasar spectra (e.g., Bouché et al. 2012; Kacprzak et al. 2015; Muzahid et al. 2015; Schroetter et al. 2015, 2016). Broad components in emission lines also pro-

vide a signature of outflows (Cicone et al. 2016; Finley et al. 2017; Concas et al. 2017; Freeman 2017), which have also recently been observed with integral-field-units spectroscopy (Davies et al. 2019; Förster Schreiber et al. 2019; Swinbank et al. 2019).

The outflows are ubiquitously observed in the star-forming galaxies at $z < 1.5$ (Weiner et al. 2009; Chen et al. 2010; Rubin et al. 2014). Their outflow velocities are probed to have a positive correlation with the star formation rate (SFR), the stellar mass (M_*), and the SFR surface density (Σ_{SFR}) (e.g., Rubin et al. 2014; Heckman & Borthakur 2016; Chisholm et al. 2016b). Sugahara et al. (2017) use archival spectra to show that maximum outflow velocity increases from $z \sim 0$ to 2 in star-forming galaxies that are in a similar M_* and SFR range.

The “down-the-barrel” technique is also appropriate for outflow studies at $z > 2$. Unlike the emission from the outflows whose detection becomes difficult toward high redshift, the absorption can be detected with a bright background continuum source. Shapley et al. (2003) construct composites of almost 1000 Lyman-break galaxy (LBG) spectra at $z \sim 3$ to discuss the relation between the FUV spectral features and the outflow properties. Recently, Du et al. (2018) report no evolution of central outflow velocities at $z \sim 2$ –4 using composites of the rest-frame FUV spectra presented in Steidel et al. (2003, 2004), Reddy et al. (2008), and Jones et al. (2012). Although the Ly α profile provides us the information on the neutral-gas kinematics around Lyman alpha emitters at high redshift (e.g., Erb et al. 2014; Shibuya et al. 2014; Hashimoto et al. 2015; Trainor et al. 2015; Karman et al. 2017), even at $z \sim 6$ (Ajiki et al. 2002), it is difficult to directly estimate the outflow properties only from the Ly α profile due to its strong resonance scattering.

One of the keys to estimate outflow properties is to determine the systemic redshifts of the galaxies. At the low redshift, the systemic redshifts are measured by nebular emission lines (e.g., H α , [O III], and [O II]), but observations of the emission lines become expensive at high redshift. Some outflow studies at $z > 1.5$ conduct additional near-infrared (IR) observations (Steidel et al. 2010; Shibuya et al. 2014), while others determine the redshifts from Ly α emission or interstellar absorption, which includes the uncertainties based on the outflows (Shapley et al. 2003; Du et al. 2018). Moreover, precise measurements of the systemic redshifts are challenging at $z > 5$, where the strong optical emission lines fall into the mid-IR bands. Although there are several nebular emission lines in the rest-frame FUV band such as O III] $\lambda\lambda 1660, 1666$ and C III] $\lambda\lambda 1906, 1908$, these lines are weak to be detected in typical star-forming galaxies at high redshift. This problem makes it difficult to extend the outflow studies to $z > 5$.

A solution in this paper is observations with the Atacama Large Millimeter/submillimeter Array (ALMA). Recent ALMA observations detect [C II] 158 μm and [O III] 88 μm emission lines in high- z galaxies (e.g., Capak et al. 2015; Inoue et al. 2016; Hashimoto et al. 2019), which enables us to measure the systemic redshifts of the galaxies. Combining

the redshift determined from the ALMA observations with deep observed-frame optical spectra, we can address the outflow properties at $z > 5$. As a case study, Pavesi et al. (2016) discuss the rest-frame FUV absorption lines in HZ10, a IR-luminous LBG at $z \simeq 5.6$, and find the blueshifts with respect to the [C II] emission line.

This paper presents estimates of outflow velocities in star-forming galaxies at $z = 5$ –6 and discuss the redshift evolution of the outflows from $z \sim 0$ to 6. Section 2 describes the sample of galaxies at $z = 5$ –6. Section 3 explains the analysis of the absorption lines in the observed-frame optical spectra. We obtain a composite spectrum of the galaxies to measure an outflow velocity. Section 4 shows the results on the outflow velocity and its redshift evolution. Section 5 discusses relations between the outflow and galaxy properties. Section 6 summarizes our conclusion. The Λ CDM cosmology is used throughout this paper: $\Omega_{\text{M}} = 0.27$, $\Omega_{\Lambda} = 0.73$, $h = H_0/(100 \text{ km s}^{-1} \text{ Mpc}^{-1}) = 0.70$, $n_s = 0.95$, and $\sigma_8 = 0.82$. All transitions are referred to by their wavelengths in vacuum.

2. SAMPLE AND DATA REDUCTION

Our sample consists of seven galaxies at $z = 5$ –6 whose spectra are taken in the optical and millimeter wavelengths. We use the galaxies presented in Capak et al. (2015), who observe nine LBGs and one low-luminosity quasar at $z \sim 5$ –6 in the Cosmic Evolution Survey (COSMOS; Scoville et al. 2007) field. Capak et al. (2015) obtain the rest-frame FUV spectra of the galaxies with the DEep Imaging Multi-Object Spectrograph (DEIMOS; Faber et al. 2003) at the Keck II telescope. The spectroscopic configuration is the 830 lines mm^{-1} grating with the OG550 filter, which gives the wavelength coverage of 6000–9500 \AA and the spectral resolution of $R \sim 2500$ –3500. The total integration time is ~ 3.5 hr for each object.

We download raw DEIMOS data of the galaxies from the Keck Observatory Archive¹ (KOA). The raw data are reduced with the IDL package, the DEIMOS spec2d pipeline, developed by the Deep Extragalactic Evolutionary Probe 2 (DEEP2) Redshift Survey team (Cooper et al. 2012; Newman et al. 2013). From the reduced two-dimensional multi-object-slit data, the pipeline extracts the one-dimensional spectra of the science targets. Finally, we obtain the rest-frame FUV spectra of seven out of the nine LBGs in Capak et al. (2015), other than two objects (HZ3 and HZ9) whose spectra we could not identify from the archive.

The ALMA follow-up observations are conducted in a project of #2012.1.00523.S (PI: P. Capak). The Band 7 observations have detected the [C II] 158 μm emission lines in all of the nine LBGs. Previous studies report possible present and past outflow signatures in the [C II] emission lines of these galaxies (Gallerani et al. 2018; Fujimoto et al. 2019). In this study, we use the systemic redshifts measured from the [C II] emission lines by Capak et al. (2015). In contrast

¹ KOA website: <http://www2.keck.hawaii.edu/koa/public/koa.php>.

Table 1. Galaxy properties of seven LBGs

name	R.A.	Decl.	S/N of DEIMOS spectra (pixel ⁻¹)	z_{sys}^a	z_{sys} error (km s ⁻¹)	$\log(M_*/M_\odot)$	$\log(\text{SFR})$ (M_\odot yr ⁻¹)	$\log(M_h/M_\odot)$	$\log(v_{\text{cir}})$ (km s ⁻¹)
HZ1	09:59:53.25	02:07:05.43	0.348115	5.6885	9	10.47 ± 0.13	$1.38^{+0.10}_{-0.06}$	$12.9^{+0.5}_{-0.5}$	$2.8^{+0.2}_{-0.2}$
HZ2	10:02:04.10	01:55:44.05	0.455985	5.6697	30	10.23 ± 0.15	$1.40^{+0.08}_{-0.04}$	$12.0^{+0.5}_{-0.3}$	$2.49^{+0.2}_{-0.08}$
HZ4	09:58:28.52	02:03:06.74	0.616747	5.5440	9	9.67 ± 0.21	$1.71^{+0.31}_{-0.19}$	$11.4^{+0.2}_{-0.1}$	$2.29^{+0.05}_{-0.04}$
HZ6	10:00:21.50	02:35:11.08	0.776667	5.2928	5	10.17 ± 0.15	$1.69^{+0.28}_{-0.12}$	$11.9^{+0.4}_{-0.2}$	$2.45^{+0.1}_{-0.07}$
HZ7	09:59:30.48	02:08:02.81	0.275164	5.2532	20	9.86 ± 0.21	$1.32^{+0.09}_{-0.04}$	$11.6^{+0.2}_{-0.1}$	$2.34^{+0.07}_{-0.05}$
HZ8	10:00:04.06	02:37:35.81	0.216720	5.1533	10	9.77 ± 0.15	$1.26^{+0.11}_{-0.05}$	$11.5^{+0.1}_{-0.1}$	$2.31^{+0.04}_{-0.03}$
HZ10	10:00:59.30	01:33:19.53	0.625486	5.6566	9	10.39 ± 0.17	$2.23^{+0.08}_{-0.08}$	$12.5^{+0.7}_{-0.5}$	$2.7^{+0.2}_{-0.2}$
composite	-	-	1.4	-	-	10.08	1.53	11.8	2.4

NOTE—The raw DEIMOS spectra are downloaded from KOA (PI: P. Capak). The z_{sys} , M_* , and SFR values are drawn from Capak et al. (2015). The M_h and v_{cir} values are estimated in Section 2. The physical parameters of the composite spectrum are the truncated mean discarding the maximum and minimum values.

^aThe systemic redshift z_{sys} is determined by the [C II] 158 μm emission line taken by ALMA.

to [O III] 88 μm or optical nebular emission lines that come from only H II regions, the [C II] emission arises from H II regions and photo-dissociated regions, which may results in some uncertainties in the measured redshifts. However, by detecting both [C II] and [O III] emission lines in objects at $z > 6$ with ALMA, recent studies reveal that redshifts determined by [C II] and [O III] are consistent within the errors (Marrone et al. 2018; Decarli et al. 2017; Walter et al. 2018) or show offsets less than 50 km s⁻¹ at most (Hashimoto et al. 2019). There is good evidence therefore that measurements of the [C II] emission lines provide reliable systemic redshifts. The median redshift error is $\sim 2 \times 10^{-4}$, corresponding to ~ 10 km s⁻¹. The systemic redshifts of our galaxies are listed in Table 1.

We use SFR and M_* derived by Capak et al. (2015). The SFR is estimated from the sum of the rest-frame UV and IR luminosity. The stellar mass M_* is estimated from the spectral energy distribution fitting to the optical to IR photometry taken from the COSMOS photometric redshift catalog (Ilbert et al. 2013) and the Spitzer-Large Area Survey with Hyper-Suprime-Cam (SPLASH; Steinhardt et al. 2014). The halo circular velocity v_{cir} is estimated from M_* . First, we convert M_* into the halo mass M_h with the stellar-to-halo mass ratio (SHMR) given by Behroozi et al. (2013), who derive the SHMR at $z = 0\text{--}8$ with the abundance matching method, although it should be noted that observational constraints are less complete and potentially less robust at $z > 4$ than at $z \lesssim 2$. Then, v_{cir} are calculated by equations in Mo & White (2002) expressed as

$$v_{\text{cir}} = \left(\frac{GM_h}{r_h} \right)^{1/2}, \quad (1)$$

$$r_h = \left(\frac{GM_h}{100\Omega_M H_0^2} \right)^{1/3} (1+z)^{-1}, \quad (2)$$

where G is the gravitational constant and r_h the halo radius.

3. ANALYSIS AND MEASUREMENTS

Because the outflowing gas gives rise to the blueshifted metal absorption lines due to the Doppler shift, the blueshift reflects the line-of-sight velocity of the outflowing gas. The absorption-line analysis requires high signal-to-noise ratios (S/N) of the continuum spectra. Our rest-frame FUV spectra have the average S/N of $\simeq 0.47$ pixel⁻¹, which is not enough for the absorption-line analysis. Therefore, we obtain a high-S/N composite spectrum by stacking all of the spectra with an inverse-variance weighted mean. The top panel of Figure 1 shows the composite spectrum and its error spectrum. The continuum S/N of the composite spectrum is 1.4 pixel⁻¹ around the Si II $\lambda 1260$ absorption line. The physical parameters of the composite spectrum are the truncated mean discarding the maximum and minimum values. We note that HZ10 has much higher SFR than other galaxies. By constructing another composite spectrum without HZ10, we check whether this high-SFR galaxy affects our results to confirm that our conclusion does not change.

In the wavelength range from 1150 to 1450 \AA in the rest frame, we use the absorption lines of Si II $\lambda 1260$, C II $\lambda 1335$, and Si IV $\lambda\lambda 1394, 1403$ for the analysis, without the Si II $\lambda 1304$ line that has a nearby strong O I $\lambda 1302$ absorption line. We hereafter refer to Si II $\lambda 1260$ as Si II.

We measure outflow velocities by fitting a line profile to the absorption lines. As the line profile, we adopt a physical profile based on the assumption of the curve of growth (Rupke et al. 2005a). This line profile $I(\lambda)$, as a function of the wavelength λ , is expressed by

$$I(\lambda)/I_0 = 1 - C_f + C_f \exp(-\tau(\lambda)), \quad (3)$$

$$\tau(\lambda) = \tau_0 \exp(-(v(\lambda) - v_0)^2/b^2), \quad (4)$$

where I_0 is the continuum level, C_f the covering fraction, $\tau(\lambda)$ the optical depth, τ_0 the optical depth at the line center, $v(\lambda)$ the velocity measured from the rest wavelength, v_0 the velocity at the line center, and b the Doppler width. The line

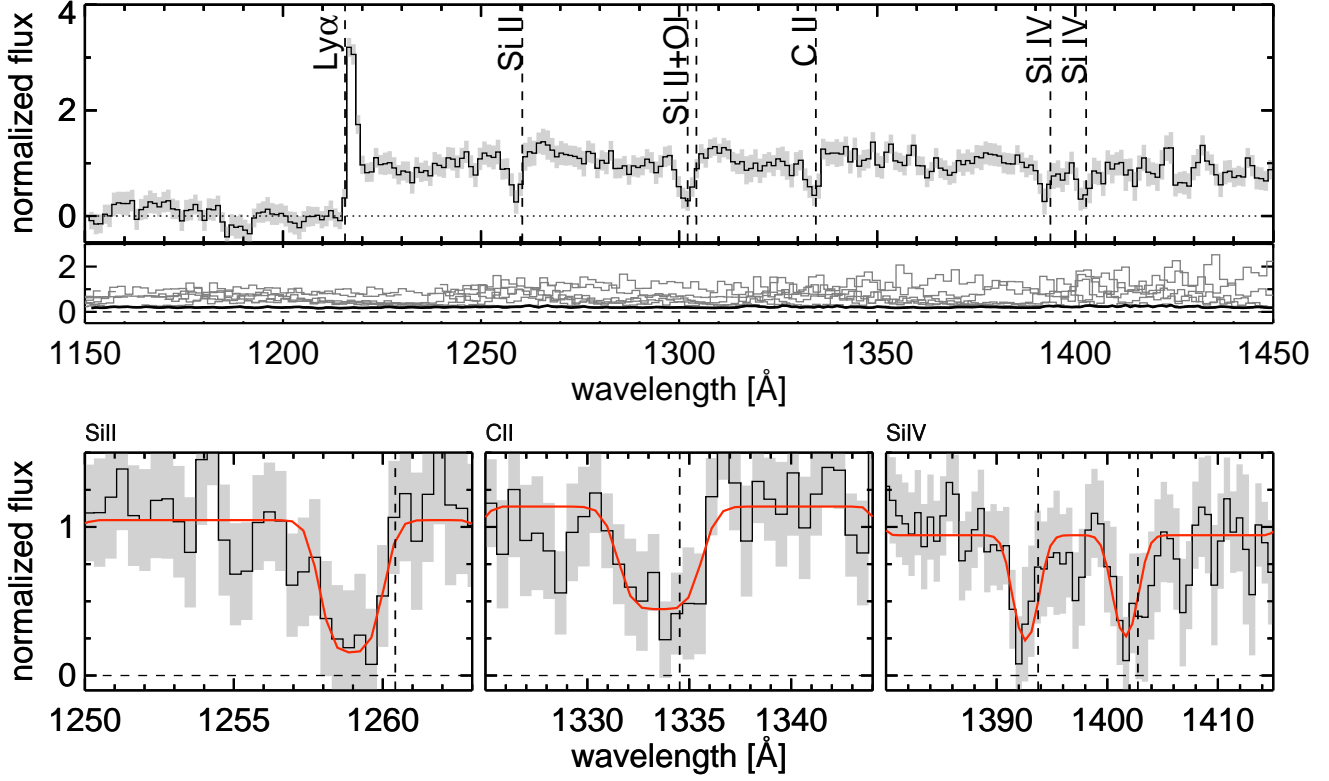


Figure 1. Top: composite spectrum of our sample. The gray shade indicates the 1σ error at each pixel. The spectral resolution is smoothed for the display purpose. The rest wavelengths of the emission and absorption lines are plotted with the dashed vertical lines. The second panel under the main panel shows the 1σ error spectra. The gray and black lines denote the errors of the normalized individual spectra and the composite spectrum, respectively. The wavelengths of the individual spectra are corrected to the rest frame using the systemic redshift determined by ALMA [C II] observation. Bottom: Si II, C II, and Si IV absorption lines from left to right. The red solid lines are the best-fit absorption model. The vertical and horizontal dashed lines denote the rest wavelengths of the absorption lines and zero flux, respectively.

profile is convolved with a Gaussian profile representing the spectral resolution. The free parameters are five: I_0 , v_0 , C_f , τ_0 , and b_D . Because the composite spectrum has large noises, we treat I_0 as a free parameter instead of normalizing the spectrum by a stellar continuum. We fit the line profile to Si II, C II, and Si IV, using an IDL procedure MPFIT, which performs non-linear least-squares fitting in a robust manner (Markwardt 2009). The bottom panel of Figure 1 shows the best-fit model of the Si II, C II, and Si IV absorption lines with the red lines.

The best-fit v_0 values, listed in Table 2, are all significantly negative, implying that the absorption lines are blueshifted by the outflowing gas. The errors of v_0 are evaluated by the parametric bootstrap method. We obtain a v_0 distribution by fitting the line profile to 1000 resampled fluxes based on the spectral noise and use the ± 34 th v_0 values for its error. These velocities are consistent with the values estimated in the literature that analyzes the data of the same galaxies (Pavesi et al. 2016; Gallerani et al. 2018). HZ10 has the Si II, Si II $\lambda 1304/\text{O I}$, and Si IV absorption lines blueshifted by $100 \pm 180 \text{ km s}^{-1}$ with respect to the [C II] emission line (Pavesi et al. 2016). The composite emission of the [C II] line in HZ1–9, without HZ5, is reported to have the broad wings

that are likely generated by the outflows with the velocity of $\sigma = 220\text{--}500 \text{ km s}^{-1}$ (Gallerani et al. 2018).

We define the maximum outflow velocity v_{max} , the highest velocity of the outflowing gas, as

$$v_{\text{max}} = -v_0 + b\sqrt{-\ln\left(\frac{1}{\tau_0} \ln \frac{1}{0.9}\right)}, \quad (5)$$

which represents the velocity where the best-fit model has a 90% flux from the continuum to the bottom of the line.² The errors of v_{max} are evaluated by the parametric bootstrap method that is the same as used to evaluate the v_0 error.

The derived maximum outflow velocities for Si II, C II, and Si IV are $v_{\text{max}}^{\text{SiII}} = 690_{-120}^{+260} \text{ km s}^{-1}$, $v_{\text{max}}^{\text{CII}} = 720_{-460}^{+140} \text{ km s}^{-1}$, and $v_{\text{max}}^{\text{SiIV}} = 610_{-96}^{+240} \text{ km s}^{-1}$, respectively. Low-ionized elements (Si II and C II) have ionization potentials lower than that of hydrogen (13.6 eV), while high-ionized elements (Si IV) have a much higher ionization potential. Although the low- and high-ionized elements trace the different state of the ISM, $v_{\text{max}}^{\text{SiII}}$ and $v_{\text{max}}^{\text{CII}}$ are consistent with $v_{\text{max}}^{\text{SiIV}}$

² Throughout this paper, v_{max} is not the maximum circular velocity in the rotation curve of a galaxy or halo, which is often used in theoretical papers.

Table 2. Measured outflow velocities for the absorption lines

redshift	line	v_0 (km s ⁻¹)	v_{\max} (km s ⁻¹)
$z = 5\text{--}6$	Si II $\lambda 1260$	-366^{+63}_{-99}	690^{+260}_{-120}
...	C II $\lambda 1335$	-210^{+120}_{-74}	720^{+140}_{-460}
...	Si IV $\lambda\lambda 1394, 1403$	-220^{+150}_{-100}	610^{+240}_{-96}
...	Si II & C II	-	700^{+180}_{-110}
$z \sim 2^a$	C II $\lambda 1335$	-175^{+13}_{-11}	673^{+35}_{-33}

^aWe obtain the velocities at $z \sim 2$ by re-analyzing the composite spectrum of Sugahara et al. (2017).

within the 1σ errors. This consistency agrees with previous work on outflows at $z \sim 0$ (Chisholm et al. 2016b).

Si II and C II have similar ionization potentials and oscillator strengths, and exhibit similar maximum outflow velocities. To obtain a typical v_{\max} value of the $z = 5\text{--}6$ galaxies, we additionally measure the maximum outflow velocity by a simultaneous fitting to Si II and C II, adopting v_{\max} as a free parameter instead of v_0 . Both lines are assumed to have the same C_f . The measured value is $v_{\max} = 700^{+180}_{-110}$ km s⁻¹. This value is consistent with v_{\max}^{SiII} and v_{\max}^{CII} , but its error is smaller than those of v_{\max}^{SiII} and v_{\max}^{CII} . Table 2 lists the measurements of v_{\max} and v_0 for each absorption lines. These v_{\max} values are consistent with the results of the [C II] emission analysis by Gallerani et al. (2018). They stack the ALMA data of HZ1–9, without HZ5, to show the highest velocity of $\sim 500\text{--}700$ km s⁻¹ at which the [C II] flux excess can be observed, although this broad flux excess may include emission from satellites around the central galaxies.

3.1. Galaxies at $z \sim 0\text{--}2$

To investigate the redshift evolution of the outflow velocity, we mainly compare the measurements at $z = 5\text{--}6$ with the results in Sugahara et al. (2017), who study outflows at $z \sim 0\text{--}2$. Here, we briefly describe the sample and analysis in Sugahara et al. (2017). They obtain outflow velocities using optical spectra of the Sloan Digital Sky Survey Data Release 7 (SDSS DR7; Abazajian et al. 2009) at $z \sim 0$, the DEEP2 DR4 survey (Newman et al. 2013) at $z \sim 1$, and the Keck/LRIS sample in Erb et al. (2006) at $z \sim 2$. The galaxies at $z \sim 0$ are the highly star-forming galaxies in which the absorption lines can be analyzed, while the galaxies at $z \sim 1$ and 2 are the star-forming main-sequence galaxies. The stellar masses of the galaxies are listed in Table 3, which are similar to the galaxies at $z = 5\text{--}6$ in this work.

Sugahara et al. (2017) basically perform the same analysis as this study. The main difference in the method is to use a two-component absorption-line profile that consists of a systemic component fixed at the systemic velocity and a blueshifted component produced by outflowing gas. This difference of the fitting profile is negligible for the spectra at $z \sim 0$ and 1, where the absorption lines have small systemic components. The spectra at $z \sim 2$, however, have

Table 3. stellar mass and outflow velocity of the galaxies in Sugahara et al. (2017)

redshift	line ^a	v_{\max} (km s ⁻¹)	$\log(M_*/M_\odot)$	symbol in figures
0.064	Na I D	221 ± 18	10.2	blue circle
0.075	Na I D	261 ± 12	10.3	blue circle
0.085	Na I D	299 ± 11	10.4	blue circle
0.11	Na I D	267 ± 11	10.5	blue circle
0.13	Na I D	327 ± 10	10.6	blue circle
0.14	Na I D	373 ± 20	10.8	blue circle
1.4	Mg II	445 ± 9	9.99	cyan diamond
1.4	Mg II	442 ± 27	10.4	cyan diamond
1.4	Mg II	569 ± 12	10.6	cyan diamond
2.2	C II	673^{+35b}_{-33}	10.3	green diamond

^aAbsorption lines that are analyzed for estimations of the v_{\max} values.

^bThe maximum outflow velocities at $z \sim 2$ are re-measured in this study.

large systemic components. We re-analyze the absorption lines of the normalized composite spectrum at $z \sim 2$ to measure the maximum outflow velocity with the one-component absorption-line profile described in Section 3. The new maximum outflow velocity becomes lower than the previous value, but the conclusions in Sugahara et al. (2017) are not affected by this re-analysis.

Although the available absorption lines differ depending on redshifts, Sugahara et al. (2017) carefully compare the outflow velocities at $z \sim 0\text{--}2$ measured from different lines and show an increase in the outflow velocities from $z \sim 0$ to 2. Table 3 lists the v_{\max} values measured from the Na I D, Mg II, and C II absorption lines for the $z \sim 0, 1,$ and 2 galaxy spectra, respectively.

4. RESULTS

4.1. Maximum Outflow Velocity vs. Galaxy Properties

Figure 2 shows the maximum outflow velocity as a function of SFR. The v_{\max}^{SiII} , v_{\max}^{CII} , v_{\max}^{SiIV} , and v_{\max} values are plotted with the open orange square, diamond, triangle, and filled red square, respectively. Sugahara et al. (2017) illustrate that the outflow velocity increases from $z \sim 0$ (blue) to 2 (green) in star-forming galaxies with similar M_* and SFR. We find that the v_{\max} value at $z = 5\text{--}6$ is ~ 0.2 dex higher than the relation at $z \sim 0$ and comparable to the value at $z \sim 2$, although the SFR values at $z \sim 0$ are not as high as those at $z = 5\text{--}6$. This means that the outflow velocity shows a strong increase from $z \sim 0$ to 2 and a slight or no increase from $z \sim 2$ to 6 in galaxies with similar M_* and SFR.

Figure 3 illustrates v_{\max} as a function of v_{cir} that are calculated from M_* in Section 2. Because the galaxies at $z = 0\text{--}6$ have similar M_* and M_h values (Table 3), the data points are

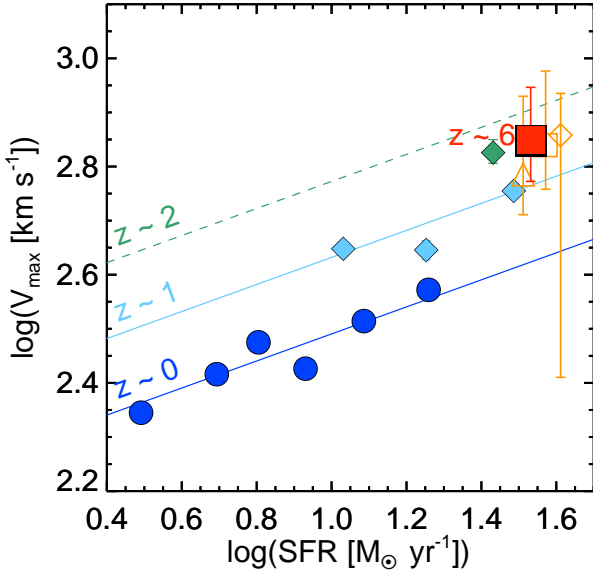


Figure 2. Maximum outflow velocity v_{\max} as a function of SFR over $z \sim 0$ –6. The filled red square indicates the v_{\max} value at $z = 5$ –6 measured with the simultaneous fitting of the Si II and C II lines. The open orange square, diamond, and triangle represent the values measured for Si II, C II, and Si IV, respectively. The data points at $z \sim 0$ (blue) and $z \sim 1$ (cyan) are presented by Sugahara et al. (2017). The v_{\max} value at $z \sim 2$ (green) is derived from the composite spectrum in Sugahara et al. (2017), but re-calculated in the manner of this work. The error bars show 1σ measurement errors. The blue, cyan, and green lines express the best-fit relations at $z \sim 0$, 1, and 2, respectively, which have slopes fixed at the best-fit value at $z \sim 0$ (Sugahara et al. 2017). There is an offset between the green diamond and the green dashed line because the $z \sim 2$ best-fit relation is the one in Sugahara et al. (2017).

located in different v_{cir} ranges depending on the redshifts. In the figure, v_{\max} tightly correlates with v_{cir} at $z \sim 0$. A correlation with a similar slope at $z \sim 0$ is also seen in the cyan diamonds at $z \sim 1$. Although only one measurement is available at $z \sim 2$ and $z = 5$ –6, respectively, the two data points at $z \sim 2$ –6 appear to follow the relation at $z \sim 0$ –1. Therefore, Figure 3 suggests a single relation between v_{\max} and v_{cir} that holds over $z \sim 0$ –6. The dotted line indicates a relation at $z = 0$ obtained from observations by the Cosmic Origin Spectrograph mounted on the Hubble Space Telescope (Heckman & Borthakur 2016), which has a similar slope to our measurements. The offset between our data points and the dotted line may arise from the fact that our data points represent the average properties of galaxies at each redshift while their extreme-starburst galaxies have much higher SFR than our galaxies.

4.2. Redshift evolution of outflow velocities

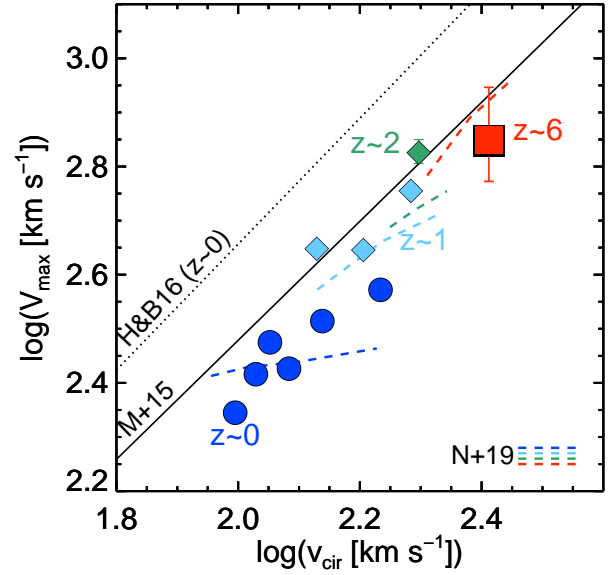


Figure 3. v_{\max} as a function of the circular velocity v_{cir} that are converted from the stellar mass. The symbols are the same as in Figure 2. The solid black line and colored dashed lines represent a theoretical relation at $z = 0.5$ –4 predicted by the FIRE simulations (the flux-weighted average 90th percentile velocity; Muratov et al. 2015) and relations at $z = 0$ (blue), 1 (cyan), 2 (green), and 6 (red) predicted by the IllustrisTNG simulation (90th percentile velocity; Nelson et al. 2019), respectively. The dotted line indicates a relation of extreme-starburst galaxies $z \sim 0$ Heckman & Borthakur (2016).

We illustrate the redshift evolution of v_{\max} in star-forming galaxies with $M_* \sim 10^{10.1} M_{\odot}$ in the top panel of Figure 4. As shown in Section 4.1, v_{\max} strongly increases from $z \sim 0$ to 2 and slightly from $z \sim 2$ to 6. Although many studies measure outflow velocities at fixed redshift, a few studies investigate the redshift evolution of the velocities in wide redshift ranges. Jones et al. (2013) present the maximum outflow velocity of gravitationally lensed sources at $z \sim 2$ –4 (cross). The stellar masses of these sources are not estimated and the outflow velocity of them is measured in a different manner from ours. However, the sources show similar outflow velocities to our v_{\max} values at $z \sim 2$ and $z = 5$ –6, except for a data point of $v_{\max} \simeq 300 \text{ km s}^{-1}$. Jones et al. (2013) suggest a decrease in v_{\max} at high redshift that is not statistically significant. We find no decrease at $z = 5$ –6.

Sugahara et al. (2017) and Du et al. (2018) discuss the redshift evolution of the central outflow velocity (v_{out}) measured with a two-component profile. While the maximum outflow velocity shows the highest velocity that the outflowing gas reaches, the central outflow velocity represents the bulk motion of the outflowing gas. Because the absorption lines include absorption components from outflows and ISM at the systemic velocity, v_{out} should be estimated by a two-component fitting. Although a two-component fit-

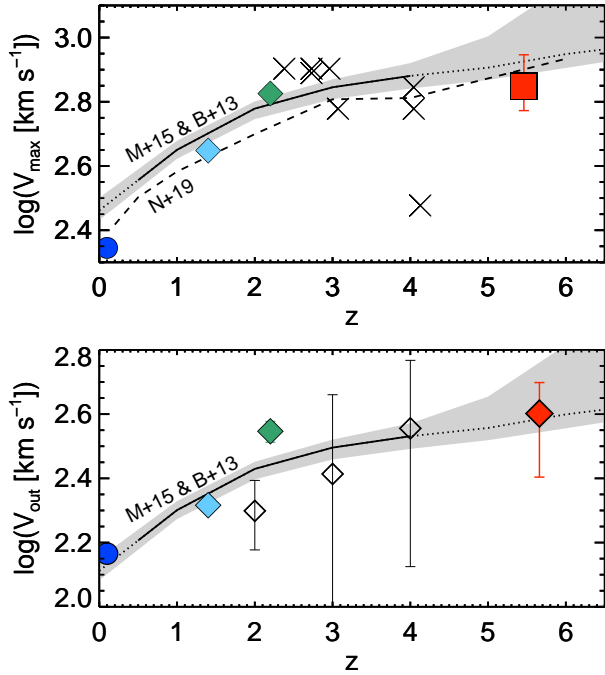


Figure 4. Redshift evolution of v_{\max} (top) and v_{out} (bottom) in the star-forming galaxies with $M_* \sim 10^{10.1} M_{\odot}$. The colored symbols are the same as in Figure 2, but for the red diamond that denotes v_{out} of the galaxies at $z = 5\text{--}6$ measured by a fit of the two-component Gaussian profile to the C II line. To compare the literature, we plot the values of the individual gravitationally-lensed sources in Jones et al. (2013, cross) and the composite spectra at $z \sim 2, 3,$ and 4 presented by Du et al. (2018, open diamond), which have the median stellar masses of $\log(M_*/M_{\odot}) = 10.00, 9.87,$ and $9.72,$ respectively. The solid lines indicate the evolution of the flux-weighted 90th (top) and 50th (bottom) outflow velocities at $M_* = 10^{10.1} M_{\odot}$ in the FIRE simulations (Muratov et al. 2015) that we convert from the velocity- v_{cir} relation at $z = 0.5\text{--}4$ using Equations (1)–(2) and the SHMR of Behroozi et al. (2013). The evolution is extrapolated to $z < 0.5$ and $z > 4$ (dotted line) and the errors of the SHMR are shown in the shaded regions. The dashed line in the top panel indicates the evolution of the 90th percentile velocity at $M_* = 10^{10.1} M_{\odot}$ in the IllustrisTNG simulation (Nelson et al. 2019).

ting produces larger errors of the best-fit values than a one-component fitting, we fit a two-component Gaussian profile to the C II absorption line in the composite spectrum at $z = 5\text{--}6$, in order to compare the v_{out} values with previous studies at $z \lesssim 4$.

The two-component Gaussian profile consists of the systemic and outflow components; v_{out} is defined as the central velocity of the outflow component. This analysis is identical to that used in Du et al. (2018). Before the fitting, the composite spectrum is smoothed by a Gaussian kernel so that the spectral resolution become similar to the composite spectrum at $z \gtrsim 2$ in Sugahara et al. (2017) and Du et al. (2018). We

Table 4. Values of the data points at each redshift in Figure 4

redshift	v_{out} (km s^{-1})	v_{\max} (km s^{-1})	$\log(M_*/M_{\odot})^a$	reference
$z \sim 0$	146 ± 5.2	221 ± 9.9	10.2	S17
$z \sim 1$	207 ± 5.0	445 ± 5.7	10.0	S17
$z \sim 2$	$352^{+26}_{-27}{}^b$	$673^{+35}_{-33}{}^b$	10.3	S17
$z = 5\text{--}6$	400^{+100}_{-150}	700^{+180}_{-110}	10.1	This study

^aThe mean stellar mass of the galaxies.

^bThe outflow velocities at $z \sim 2$ are re-measured in this study.

References—S17: Sugahara et al. (2017)

also analyze the composite spectrum at $z \sim 2$ presented in Sugahara et al. (2017).

The measured velocities are $v_{\text{out}} = 400^{+100}_{-150} \text{ km s}^{-1}$ at $z = 5\text{--}6$ and $v_{\text{out}} = 352^{+26}_{-27} \text{ km s}^{-1}$ at $z \sim 2$. In the bottom panel of Figure 4, we plot the measured v_{out} values, showing that the v_{out} redshift evolution has similar features to the v_{\max} evolution: a strong increase from $z \sim 0$ to 2 and no increase from $z \sim 2$ to 6 within the errors. The latter is consistent with a result of Du et al. (2018). The v_{\max} and v_{out} values at $z \sim 0, 1, 2,$ and $5\text{--}6$ are listed in Table 4.

The open diamonds indicate v_{out} at $z \sim 2, 3,$ and 4 given by Du et al. (2018). The v_{out} value at $z = 5\text{--}6$ is comparable to those at $z \sim 3$ and 4 within the marginally large error bars. However, the value at $z \sim 2$ denoted by the green diamond is not consistent with the one denoted by the open diamond. In addition, the error bars of the open diamonds are generally larger than those of the filled symbols, in spite of the fact that Du et al. (2018) stacked a larger number of galaxy spectra than this study and Sugahara et al. (2017). These results may be attributed to the uncertainty of the systemic redshifts in Du et al. (2018), who determine the systemic redshifts from the Ly α emission or interstellar absorption lines. When individual spectra are stacked using the systemic redshifts, the uncertainties of the systemic redshifts broaden absorption lines in the composite spectrum. It is possible that this broadened absorption line produces low values and large errors of the best-fit parameters measured with the two-component fitting, which are sensitive to absorption-line profiles. We note that the median stellar masses of the galaxies in Du et al. (2018) are $\log(M_*/M_{\odot}) = 10.00, 9.87,$ and 9.72 at $z \sim 2, 3,$ and $4,$ respectively, which are less than M_* of our galaxies. It is also possible that this small M_* (i.e., small v_{cir}) may lead to the low v_{out} value at $z \sim 2$.

5. DISCUSSION

5.1. Comparisons with theoretical models

Recent numerical and zoom-in simulations can be used to predict outflow velocities. These simulations compute energy input to the ISM surrounding SNe and investigate the statistics of galaxy and outflow properties (e.g., Muratov et al. 2015; Christensen et al. 2016; Mitchell et al. 2018;

Nelson et al. 2019). Here we compare our results with simulation work that studies the redshift evolution of the outflow velocities. In the figures we convert $M_*(v_{\text{cir}})$ into $v_{\text{cir}}(M_*)$ in the simulation work by using Equations (1)–(2) and the SHMR in Behroozi et al. (2013).

Nelson et al. (2019) analyze $\sim 20,000$ galaxies in the IllustrisTNG simulation to provide statistical relations between outflow and galaxy properties, including SN and AGN feedback. Figure 3 shows outflow velocities, $v_{\text{out},90,r=10 \text{ kpc}}$, defined as the 90th percentile of the flux-weighted velocity distribution at a radius of 10 kpc, at $z = 0.2, 1, 2$, and 6 in stellar mass ranges similar to observational data points at the redshifts. This theoretical prediction by Nelson et al. (2019) agrees well with our observational measurements, although the trend at $z \sim 0$ is different.

Muratov et al. (2015) calculate the flux-weighted velocity of the outflowing gas at one quarter of the halo virial radius with the Feedback in Realistic Environments (FIRE) simulations, which computes the thermal and momentum input to the ISM considering the stellar and SN feedback. The outflow velocity in the FIRE simulations tightly correlates with the halo circular velocity and the correlation does not exhibit the significant evolution over $z \sim 0.5\text{--}4$. Figure 3 illustrates that the correlation in the FIRE simulations at $z = 0.5\text{--}4$ is in good agreement with the tight linear relation which we present in Section 4.1, although the outflow velocity at $z \sim 0$ is ~ 0.1 dex lower than the theoretical prediction.

These agreements with theoretical work support our result that v_{max} correlates with v_{cir} in a given stellar mass range. However, we note two factors that are important when one compares observations and theories: gas phases and galactocentric radii of outflows. As described in Section 3 our observational technique traces low-ionized elements in warm gas ($\lesssim 10^4$ K). On the other hand, Muratov et al. (2015) and Nelson et al. (2019) compute the $v_{\text{max}}\text{--}v_{\text{cir}}(M_*)$ relation from outflowing gas with all temperatures. It is noteworthy that a non-negligible fraction of outflowing gas in numerical simulations would be in a hot, diffuse phase which are not observable with optical absorption lines (e.g., Mitchell et al. 2018; Nelson et al. 2019). Moreover, in some numerical simulations, outflows in a hot phase tend to exhibit faster velocities than those in cold phases (e.g., Gallerani et al. 2018; Mitchell et al. 2018). In addition to gas phases, galactocentric distances of outflowing gas are different between observations and simulations. Observations with the “down-the-barrel” technique integrate outflowing-gas absorption along the line of sight and cannot distinguish absorption components at different radii, while most simulations compute outflow velocities at fixed radii. Even among the simulations, Nelson et al. (2019) and Muratov et al. (2015) compute velocities at different radii, 10 kpc and 0.25 halo virial radius, respectively, despite a radial dependence of outflow velocities (Nelson et al. 2019). Considering these all factors, it is difficult to interpret the similar $v_{\text{max}}\text{--}v_{\text{cir}}$ relation in this work, Nelson et al. (2019), and Muratov et al. (2015). Nevertheless, the agreement perhaps suggests that multi-phase

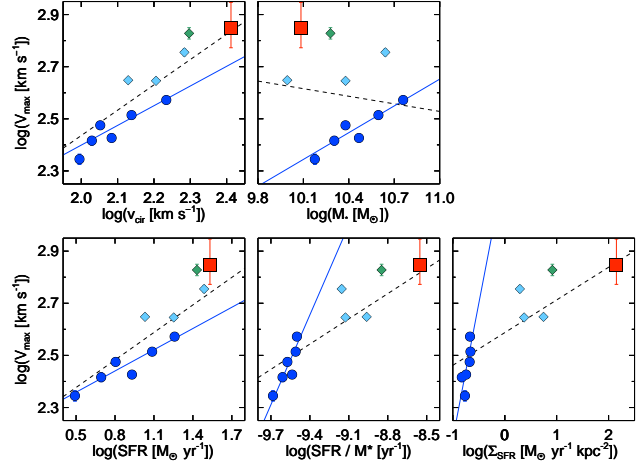


Figure 5. Correlations between v_{max} and galaxy properties. The symbols are the same as in Figure 2. The blue solid lines indicate the best-fit linear relations to the data points at $z \sim 0$. The black dashed lines denote the best-fit linear relations to the data points throughout all redshifts.

outflows are accelerated following a common $v_{\text{max}}\text{--}v_{\text{cir}}$ relation, irrespective of gas phases.

In Figure 4 the black solid and dot-dashed lines indicate the redshift evolution of predicted outflow velocities at $M_* = 10^{10.1} M_\odot$ based on the results given by the FIRE (Muratov et al. 2015) and the IllustrisTNG (Nelson et al. 2019) simulations, respectively. The evolution based on the simulations is in good agreement with the v_{max} and v_{out} values in this study and Sugahara et al. (2017), and also with those in Du et al. (2018) and Jones et al. (2013), except for one at $z \sim 4$.

These simulations support a monotonic increase in v_{max} from $z = 0$ to 6 at a fixed stellar mass of $M_* \sim 10^{10.1} M_\odot$. This increase will be explained by a monotonic increase in v_{cir} . While M_h does not significantly change around $M_* \sim 10^{10.1} M_\odot$ at $z \sim 0\text{--}6$ (Behroozi et al. 2013), r_h is proportional to $(1+z)^{-1}$ at a fixed M_h (Equation 2). Hence, Equation (1) gives the redshift dependence of the halo circular velocity as $v_{\text{cir}} \propto (1+z)^{0.5}$. Given that v_{max} has the linear correlation with v_{cir} as shown in Figure 3, the redshift evolution in v_{max} (Figure 4) is explained as reflecting the redshift dependence of v_{cir} . The power-law index of 0.5 reproduces the strong increase in v_{max} from $z \sim 0$ to 2 and the slight increase from $z \sim 2$ to 6.

5.2. Outflow-velocity correlation with SFR

The outflow maximum velocity tightly correlates with the halo circular velocity, but it also has a strong correlation with SFR. To study the fundamental parameter that determines the outflow velocity over all redshifts, it is worth discussing correlations of v_{max} with galaxy properties over the wide redshift range. If there exists the fundamental parameter, it should exhibit a single scaling relation with v_{max} that holds at fixed redshifts and throughout all redshifts.

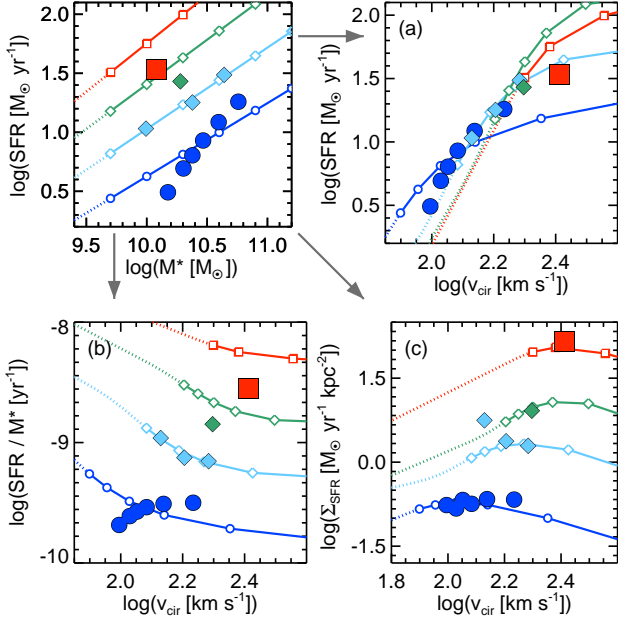


Figure 6. Models of the correlations of SFR, SFR/M_* , and Σ_{SFR} with v_{cir} for the star-forming main-sequence galaxies. The top left panel shows the main sequences at $z \sim 0.5$ (blue), 1 (cyan), 2 (green), and 6 (red) that are presented by Speagle et al. (2014). The open symbols on the solid lines are plotted at the intervals of 0.3 dex of M_* for reference. The main sequences are extrapolated to $\log(M_*/M_\odot) < 9.7$, indicated by the dotted lines. The filled symbols are the same as in Figure 2. (a) SFR versus v_{cir} where v_{cir} is converted from M_* in the top panel using the SHMR in Behroozi et al. (2013). SFR correlates with v_{cir} over $z = 0-6$. (b) SFR/M_* versus v_{cir} . (c) Σ_{SFR} versus v_{cir} ; Σ_{SFR} is estimated on the assumption that galaxy sizes are proportional to redshifts by $(1+z)^{-1}$ (Shibuya et al. 2015). In the panels (b) and (c), the colored data points, which are in a similar M_* range, exhibit positive correlations. However, the solid lines demonstrate that the relations of the main-sequence galaxies depend on redshifts. Given a $v_{cir}-v_{max}$ correlation, the panels (b) and (c) suggest that SFR/M_* and Σ_{SFR} are unlikely to be the fundamental parameter.

Figure 5 plots v_{max} as a function of v_{cir} , M_* , SFR, SFR/M_* , and Σ_{SFR} . Because galaxy sizes are unavailable at high- z due to the spacial resolutions, Σ_{SFR} is estimated on the assumption that galaxy sizes are proportional to redshifts by $(1+z)^{-1}$ (Shibuya et al. 2015). First, we calculate the Spearman’s rank correlations, r , between v_{max} and the galaxy properties over all redshifts. While M_* has no correlation with v_{max} , the other galaxy properties exhibit strong correlations of $r = 0.81$ (v_{cir}), 0.78 (SFR), 0.90 (SFR/M_*), and 0.89 (Σ_{SFR}) with the $> 3\sigma$ significance levels. Next, we perform a linear fitting to the data points at all redshifts and only at $z \sim 0$. The best-fit results are illustrated in Figure 5. The best-fit slopes at all redshifts (black line) are positive for v_{cir} , SFR, SFR/M_* , and Σ_{SFR} . For v_{cir} and SFR, the data points show relatively small scatter within ~ 0.1 dex with re-

spect to the best-fit relation at all redshifts. For SFR/M_* and Σ_{SFR} , however, the best-fit relations at $z \sim 0$ (blue line) have large offsets from the data points at $z \sim 1-6$, and the slopes of the best-fit relations at $z \sim 0$ and at all redshifts are very different from each other. These correlation and linear-fitting tests demonstrate that M_* , SFR/M_* and Σ_{SFR} show scaling relations at $z \sim 0$, but those scaling relations cannot explain the outflow velocity throughout all redshifts. Therefore, v_{cir} and SFR are likely to have the tightest single relations with v_{max} from $z \sim 0$ to 6.

The strong v_{max} -correlations with v_{cir} and SFR imply a strong correlation between v_{cir} and SFR. To understand the SFR- v_{cir} relation independent of redshifts, it is helpful to see the distribution of the star-forming main-sequence galaxies on a SFR- v_{cir} plane. The top left panel of Figure 6 illustrates the main sequences at $z \sim 0.5, 1, 2$, and 6 that are presented by Speagle et al. (2014). The galaxies in this work and Sugahara et al. (2017) have similar stellar masses in the range of $10.0 < \log(M_*/M_\odot) < 11.0$. We note that the main sequence at $z \sim 0.5$ (blue line) agrees with galaxies at $z \sim 0.1$ (blue circles) because Sugahara et al. (2017) construct the $z \sim 0$ sample with the highly star-forming galaxies to analyze the Na I D absorption line. By converting M_* into v_{cir} with the method in Section 2, we plot the main sequences on a SFR- v_{cir} plane in the panel (a) of Figure 6. They show similar positive relations at all redshifts, leading to a positive correlation of the main-sequence galaxies, irrespective of redshifts. The data points indeed exhibit a strong positive correlation ($r = 0.99$) at the 5.8σ significance level. This result naturally explains that v_{max} has a correlation with v_{cir} and SFR simultaneously. In other words, constraining the fundamental parameter requires more measurements in a wide range of the stellar masses, SFR, and redshifts.

In the panels (b) and (c) of Figure 6, we plot the main sequences on SFR/M_*-v_{cir} and $\Sigma_{SFR}-v_{cir}$ planes, respectively, which are useful to understand Figure 5. Contrary to those on the SFR- v_{cir} plane, the main sequences have offsets in the positive direction from low to high redshifts. This demonstrates that the apparent positive correlation of the data points on the SFR/M_*-v_{cir} and $\Sigma_{SFR}-v_{cir}$ planes are simply because the galaxies have the similar stellar masses. Given a redshift-independent correlation between v_{cir} and v_{max} as discussed above, Figure 6 illustrates scaling relations between v_{max} and galaxy properties at each redshift, which clearly reproduces the distribution of the data points in Figure 5. These simple models suggest that $v_{max}-SFR/M_*$ and $v_{max}-\Sigma_{SFR}$ relations of the main-sequence galaxies depend on redshifts, namely, that SFR/M_* and Σ_{SFR} are unlikely to be the fundamental parameter.

The parameters which most strongly correlate with v_{max} are v_{cir} and SFR, suggesting that the fundamental parameter is v_{cir} or SFR. This result agrees with previous observational studies that present positive correlations of v_{max} with M_* (Martin 2005; Rubin et al. 2014; Erb et al. 2012) or SFR (Kornei et al. 2012; Heckman et al. 2015; Heckman & Borthakur 2016). In many cases, the outflow properties are assumed to be connected with star-forming activities in

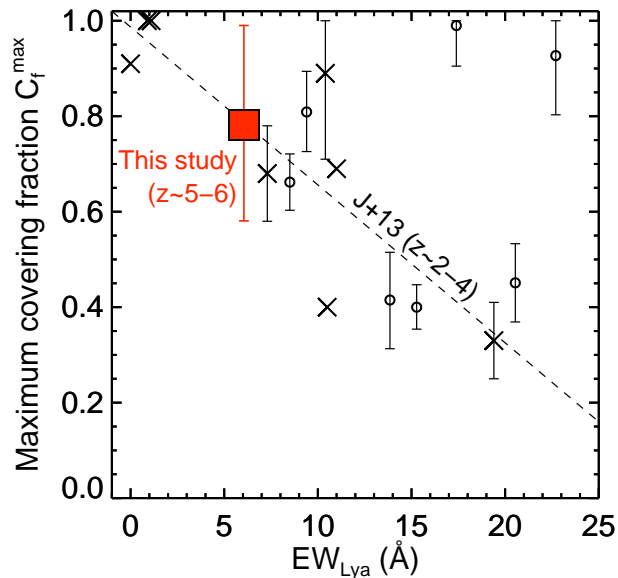


Figure 7. The maximum covering fraction C_f^{\max} as a function of the Ly α equivalent width. The red square denotes the result at $z = 5-6$. The crosses and the open circles indicate the values of gravitationally-lensed sources at $z \sim 2-4$ (Jones et al. 2013) and $z \sim 4-5$ (Leethochawalit et al. 2016), respectively. The dashed line is the best-fit linear relation to the crosses (Jones et al. 2013).

galaxies. However, v_{cir} affects SFR through the halo accretion rate (e.g., Harikane et al. 2018; Tacchella et al. 2018) and this process contributes to form the SFR- v_{cir} correlation in Figure 6. Thus, because v_{cir} represents two key parameters for the outflow velocity, the gravitational potential and the star-forming activity, it is important to consider the possibility that v_{cir} is the fundamental parameter to determine the outflow velocity.

5.3. Lyman-continuum leakage

The redshift $z = 5-6$ is near the end of the cosmic reionization, when the neutral IGM has been ionized. Plausible ionizing sources are young, low-mass galaxies (e.g., Robertson et al. 2015; Ishigaki et al. 2018), but their contribution is still a matter of debate. A key physical parameter is the escape fraction of the Lyman-continuum (LyC) photons from galaxies (f_{esc}). Because it is possible that the outflows help increase f_{esc} by creating holes in the neutral ISM from which the LyC photons can escape, the high- z galaxies with outflows in this work are appropriate for the reionization study. However, direct measurements of f_{esc} are challenging for galaxies at $z = 5-6$ because the LyC photons almost disappear by ionizing the neutral IGM. In this section, we discuss the f_{esc} value of our galaxies at $z = 5-6$ with two indirect methods regarding the absorption lines.

In the first method, we calculate the covering fraction from the metal absorption lines. In cases of the optically-thick out-

flowing gas, absorption lines are saturated and the line depth gives the covering fractions. Assuming that the low-ionized elements are associated with the neutral-hydrogen gas, Jones et al. (2013) evaluate the maximum covering fraction (C_f^{\max}) of the low-ionized elements from the low-ionized absorption lines as an upper limit of f_{esc} . Because our composite spectrum has the low continuum S/N, we define C_f^{\max} as $C_f^{\max} = 1 - F_{\text{SiII}}$, where F_{SiII} is the median flux density of the Si II line from -350 to -100 km s $^{-1}$ in the normalized spectrum. Its error is calculated with the parametric bootstrap method based on the spectral noise. The measured value is $C_f^{\max} = 0.8 \pm 0.2$. We note that this C_f^{\max} value is likely smaller than the value evaluated by the method in Jones et al. (2013) because our C_f^{\max} value is calculated in the wide velocity range of 250 km s $^{-1}$. We additionally measure the Ly α equivalent width ($\text{EW}_{\text{Ly}\alpha}$) of the composite spectrum to be $\text{EW}_{\text{Ly}\alpha} = 6.05 \pm 0.45$ Å, using the emission strength from the stellar continuum at 1216–1221 Å.

Figure 7 illustrates C_f^{\max} as a function of $\text{EW}_{\text{Ly}\alpha}$. Our measurement at $z = 5-6$ (red square) is consistent with previous results (Jones et al. 2013; Leethochawalit et al. 2016) and on the linear relation at $z \sim 2-4$ presented by Jones et al. (2013, dashed line). This is the first observational result showing that the linear relation between C_f^{\max} and $\text{EW}_{\text{Ly}\alpha}$ holds even at $z > 5$, provided that the relation is independent of the stellar mass. Using the C_f^{\max} value corresponding to $\text{EW}_{\text{Ly}\alpha} = 6.05$ Å on the relation, we obtain an upper limit of f_{esc} to be $\simeq 0.2$. This secure upper limit is too weak to constrain models where bright galaxies contribute to the cosmic reionization (e.g., $\sim 10\%$; Sharma et al. 2017). However, Jones et al. (2013) emphasize that the property derived by this method is an upper limit. Following an equation derived by Chisholm et al. (2018), who propose indirect estimations of f_{esc} using local LyC leaking galaxies, we obtain $f_{\text{esc}} \lesssim 0.5 - 0.6C_f^{\max} = 0.02$. Hence, the intrinsic f_{esc} is likely much lower than the upper-limit value.

In the second method, we consider the shape of the absorption-line profile using the outflow velocities. Chisholm et al. (2017) calculate the ratio of the maximum outflow velocity to the central outflow velocity (v_{90}/v_{cen}) of galaxies at $z = 0$. They find that the LyC leaking galaxies exhibit smaller ratios, $v_{90}/v_{\text{cen}} \lesssim 5$, than galaxies without LyC leakage, although there are several galaxies with $v_{90}/v_{\text{cen}} < 5$ but $f_{\text{esc}} = 0$. Here we use $|v_{\text{max}}/v_0|$ for an alternative to v_{90}/v_{cen} used in Chisholm et al. (2017). The ratio for the galaxies at $z = 5-6$ is obtained to be $|v_{\text{max}}/v_0| = 2.0 \pm 0.2$. This result suggests that the galaxies at $z = 5-6$ are the LyC leaking galaxies, in contrast to the result of the first method. Further studies on both the LyC photons and the absorption-line properties will provide key quantities to address the challenge of estimating f_{esc} for galaxies at the epoch of reionization.

6. CONCLUSION

We study the outflow velocities of star-forming galaxies at $z = 5-6$ and discuss the redshift evolution of the outflow ve-

locities from $z \sim 0$ to 6 by analyzing rest-frame FUV spectra of seven LBGs at $z = 5-6$ taken by DEIMOS available to date. We construct a high-S/N composite FUV spectrum based on the systemic redshifts determined by ALMA [C II] 158 μm observations (Capak et al. 2015) to fit a line profile to the Si II $\lambda 1260$, C II $\lambda 1335$, and Si IV $\lambda\lambda 1394, 1403$ absorption lines. One of the best-fit parameters v_0 , the central velocity of the line profile, is significantly negative, which implies that the absorption lines are blueshifted by the outflows.

The maximum outflow velocity v_{max} is measured from the best-fit parameters. The v_{max} values for the low-ionized lines (Si II and C II) are comparable to the one for the high-ionized line (Si IV), within the moderately large errors. By a simultaneous fit to the Si II and C II lines, we obtain $v_{\text{max}} = 700_{-110}^{+180}$ km s^{-1} , which is higher than those at $z \sim 0$ and comparable to the one at $z \sim 2$ presented by Sugahara et al. (2017). This result represents the redshift evolution of v_{max} that strongly increases from $z \sim 0$ to 2 and weakly increases from $z \sim 2$ to 6, at the fixed stellar mass of $\log(M_*/M_\odot) \sim 10.1$. We additionally measure the central outflow velocity (v_{out}) by fitting a two-component Gaussian profile to the C II line, and confirm that the redshift evolution of v_{out} is similar to the v_{max} evolution.

Over $z \sim 0-6$, $\log v_{\text{max}}$ is linearly correlated with the halo circular velocity ($\log v_{\text{cir}}$) that are estimated from the stellar mass. This linear correlation can explain the increasing features of the v_{max} evolution because v_{cir} is proportional to $(1+z)^{0.5}$ for the galaxies with $\log(M_*/M_\odot) \sim 10.1$, at which the halo mass is almost constant over $z \sim 0-6$ (Behroozi et al. 2013). In addition, the correlation between v_{max} and v_{cir} is in good agreement with a relation predicted by the IllustrisTNG (Nelson et al. 2019) and the FIRE (Muratov et al. 2015) simulations. Although there are differences of gas phases and galactocentric radii between the simulation and observational work, this good agreement perhaps suggest that the multi-phase outflows are driven by a common $v_{\text{max}}-v_{\text{cir}}$ relation.

The outflow maximum velocity v_{max} strongly correlates with v_{cir} , SFR, SFR/M_* , and Σ_{SFR} over $z = 0-6$. Moreover, on the $v_{\text{max}}-v_{\text{cir}}$ and $v_{\text{max}}-\text{SFR}$ planes, the linear scaling relations at $z = 0$ explain the whole distribution from

$z = 0$ to 6. Given that the $v_{\text{max}}-v_{\text{cir}}$ relation holds at any redshifts, the models of the star-forming main sequences reproduce the relation between v_{max} and galaxy properties at $z = 0-6$. For these reasons, v_{cir} or SFR are likely to be the fundamental parameter to determine v_{max} with a single relation throughout all redshifts. Considering that v_{cir} has an impact on SFR through the halo accretion rate, it is possible that v_{cir} is the fundamental parameter.

Absorption-line profiles are also used for indirect estimations of the escape fraction of the LyC photons (f_{esc}). We find that the maximum covering fraction of the Si II line and the Ly α equivalent width of the composite spectrum at $z = 5-6$ are consistent with a relation at $z \sim 2-4$. The intrinsic f_{esc} would be much lower than the secure upper limit $f_{\text{esc}} < 0.2$, while the ratio $|v_{\text{max}}/v_0|$ is comparable to the values of the local LyC leaking galaxies.

We thank Xinnan Du, Kate Rubin, John Chisholm, Léo Michel-Dansac, Timothy M. Heckman, and Hidenobu Yajima for very useful discussion and comments. We wish to thank the referee for constructive and valuable suggestions for improvement. We acknowledge Peter Capak, the PI of the data in this work. The data presented herein were obtained at the W. M. Keck Observatory, which is operated as a scientific partnership among the California Institute of Technology, the University of California and the National Aeronautics and Space Administration. The Observatory was made possible by the generous financial support of the W. M. Keck Foundation. This research has made use of the Keck Observatory Archive (KOA), which is operated by the W. M. Keck Observatory and the NASA Exoplanet Science Institute (NExScI), under contract with the National Aeronautics and Space Administration. The authors wish to recognize and acknowledge the very significant cultural role and reverence that the summit of Maunakea has always had within the indigenous Hawaiian community. We are most fortunate to have the opportunity to conduct observations from this mountain. This work is supported by World Premier International Research Center Initiative (WPI Initiative), MEXT, Japan, and KAKENHI (15H02064, 17H01110, and 17H01114) Grant-in-Aid for Scientific Research (A) through Japan Society for the Promotion of Science. Y.S. acknowledges support from the JSPS through the JSPS Research Fellowship for Young Scientists.

REFERENCES

- Abazajian, K. N., Adelman-McCarthy, J. K., Agüeros, M. A., et al. 2009, *ApJS*, 182, 543, doi: [10.1088/0067-0049/182/2/543](https://doi.org/10.1088/0067-0049/182/2/543)
- Ajiki, M., Taniguchi, Y., Murayama, T., et al. 2002, *ApJL*, 576, L25, doi: [10.1086/343026](https://doi.org/10.1086/343026)
- Behroozi, P. S., Wechsler, R. H., & Conroy, C. 2013, *ApJ*, 770, 57, doi: [10.1088/0004-637X/770/1/57](https://doi.org/10.1088/0004-637X/770/1/57)
- Bouché, N., Hohensee, W., Vargas, R., et al. 2012, *MNRAS*, 426, 801, doi: [10.1111/j.1365-2966.2012.21114.x](https://doi.org/10.1111/j.1365-2966.2012.21114.x)
- Capak, P. L., Carilli, C., Jones, G., et al. 2015, *Nature*, 522, 455, doi: [10.1038/nature14500](https://doi.org/10.1038/nature14500)
- Ceverino, D., Arribas, S., Colina, L., et al. 2016, *MNRAS*, 460, 2731, doi: [10.1093/mnras/stw1195](https://doi.org/10.1093/mnras/stw1195)
- Chen, Y.-M., Tremonti, C. A., Heckman, T. M., et al. 2010, *AJ*, 140, 445, doi: [10.1088/0004-6256/140/2/445](https://doi.org/10.1088/0004-6256/140/2/445)
- Chisholm, J., Orlitová, I., Schaerer, D., et al. 2017, *A&A*, 605, A67, doi: [10.1051/0004-6361/201730610](https://doi.org/10.1051/0004-6361/201730610)

- Chisholm, J., Tremonti, C. A., Leitherer, C., & Chen, Y. 2016a, MNRAS, 463, 541, doi: [10.1093/mnras/stw1951](https://doi.org/10.1093/mnras/stw1951)
- Chisholm, J., Tremonti, C. A., Leitherer, C., Chen, Y., & Wofford, A. 2016b, MNRAS, 457, 3133, doi: [10.1093/mnras/stw178](https://doi.org/10.1093/mnras/stw178)
- Chisholm, J., Tremonti, C. A., Leitherer, C., et al. 2015, ApJ, 811, 149, doi: [10.1088/0004-637X/811/2/149](https://doi.org/10.1088/0004-637X/811/2/149)
- Chisholm, J., Gazagnes, S., Schaerer, D., et al. 2018, A&A, 616, A30, doi: [10.1051/0004-6361/201832758](https://doi.org/10.1051/0004-6361/201832758)
- Christensen, C. R., Davé, R., Governato, F., et al. 2016, ApJ, 824, 57, doi: [10.3847/0004-637X/824/1/57](https://doi.org/10.3847/0004-637X/824/1/57)
- Cicone, C., Maiolino, R., & Marconi, A. 2016, A&A, 588, A41, doi: [10.1051/0004-6361/201424514](https://doi.org/10.1051/0004-6361/201424514)
- Concas, A., Popesso, P., Brusa, M., et al. 2017, A&A, 606, A36, doi: [10.1051/0004-6361/201629519](https://doi.org/10.1051/0004-6361/201629519)
- Concas, A., Popesso, P., Brusa, M., Mainieri, V., & Thomas, D. 2019, A&A, 622, A188, doi: [10.1051/0004-6361/201732152](https://doi.org/10.1051/0004-6361/201732152)
- Cooper, M. C., Newman, J. A., Davis, M., Finkbeiner, D. P., & Gerke, B. F. 2012, ASCL. <http://ascl.net/1203.003>
- Davies, R. L., Förster Schreiber, N. M., Übler, H., et al. 2019, ApJ, 873, 122, doi: [10.3847/1538-4357/ab06f1](https://doi.org/10.3847/1538-4357/ab06f1)
- Dayal, P., & Ferrara, A. 2018, PhR, 780, 1, doi: [10.1016/j.physrep.2018.10.002](https://doi.org/10.1016/j.physrep.2018.10.002)
- Decarli, R., Walter, F., Venemans, B. P., et al. 2017, Nature, 545, 457, doi: [10.1038/nature22358](https://doi.org/10.1038/nature22358)
- Du, X., Shapley, A. E., Reddy, N. A., et al. 2018, ApJ, 860, 75, doi: [10.3847/1538-4357/aabfcf](https://doi.org/10.3847/1538-4357/aabfcf)
- Erb, D. K., Quider, A. M., Henry, A. L., & Martin, C. L. 2012, ApJ, 759, 26, doi: [10.1088/0004-637X/759/1/26](https://doi.org/10.1088/0004-637X/759/1/26)
- Erb, D. K., Steidel, C. C., Shapley, A. E., et al. 2006, ApJ, 647, 128, doi: [10.1086/505341](https://doi.org/10.1086/505341)
- Erb, D. K., Steidel, C. C., Trainor, R. F., et al. 2014, ApJ, 795, 33, doi: [10.1088/0004-637X/795/1/33](https://doi.org/10.1088/0004-637X/795/1/33)
- Faber, S. M., Phillips, A. C., Kibrick, R. I., et al. 2003, in Proc. SPIE, Vol. 4841, Instrument Design and Performance for Optical/Infrared Ground-based Telescopes, ed. M. Iye & A. F. M. Moorwood, 1657–1669
- Finley, H., Bouché, N., Contini, T., et al. 2017, A&A, 605, A118, doi: [10.1051/0004-6361/201730428](https://doi.org/10.1051/0004-6361/201730428)
- Förster Schreiber, N. M., Übler, H., Davies, R. L., et al. 2019, ApJ, 875, 21, doi: [10.3847/1538-4357/ab0ca2](https://doi.org/10.3847/1538-4357/ab0ca2)
- Freeman, K. C. 2017, ARA&A, 55, 1, doi: [10.1146/annurev-astro-091916-055249](https://doi.org/10.1146/annurev-astro-091916-055249)
- Fujimoto, S., Ouchi, M., Ferrara, A., et al. 2019, arXiv e-prints. <https://arxiv.org/abs/1902.06760>
- Gallerani, S., Pallottini, A., Feruglio, C., et al. 2018, MNRAS, 473, 1909, doi: [10.1093/mnras/stx2458](https://doi.org/10.1093/mnras/stx2458)
- Harikane, Y., Ouchi, M., Ono, Y., et al. 2018, PASJ, 70, S11, doi: [10.1093/pasj/psx097](https://doi.org/10.1093/pasj/psx097)
- Hashimoto, T., Verhamme, A., Ouchi, M., et al. 2015, ApJ, 812, 157, doi: [10.1088/0004-637X/812/2/157](https://doi.org/10.1088/0004-637X/812/2/157)
- Hashimoto, T., Inoue, A. K., Mawatari, K., et al. 2019, PASJ, 71, 71, doi: [10.1093/pasj/psz049](https://doi.org/10.1093/pasj/psz049)
- Heckman, T. M., Alexandroff, R. M., Borthakur, S., Overzier, R., & Leitherer, C. 2015, ApJ, 809, 147, doi: [10.1088/0004-637X/809/2/147](https://doi.org/10.1088/0004-637X/809/2/147)
- Heckman, T. M., & Borthakur, S. 2016, ApJ, 822, 9, doi: [10.3847/0004-637X/822/1/9](https://doi.org/10.3847/0004-637X/822/1/9)
- Heckman, T. M., Lehnert, M. D., Strickland, D. K., & Armus, L. 2000, ApJS, 129, 493, doi: [10.1086/313421](https://doi.org/10.1086/313421)
- Ilbert, O., McCracken, H. J., Le Fèvre, O., et al. 2013, A&A, 556, A55, doi: [10.1051/0004-6361/201321100](https://doi.org/10.1051/0004-6361/201321100)
- Inoue, A. K., Tamura, Y., Matsuo, H., et al. 2016, Science, 352, 1559, doi: [10.1126/science.aaf0714](https://doi.org/10.1126/science.aaf0714)
- Ishigaki, M., Kawamata, R., Ouchi, M., et al. 2018, ApJ, 854, 73, doi: [10.3847/1538-4357/aaa544](https://doi.org/10.3847/1538-4357/aaa544)
- Jones, T., Stark, D. P., & Ellis, R. S. 2012, ApJ, 751, 51, doi: [10.1088/0004-637X/751/1/51](https://doi.org/10.1088/0004-637X/751/1/51)
- Jones, T. A., Ellis, R. S., Schenker, M. A., & Stark, D. P. 2013, ApJ, 779, 52, doi: [10.1088/0004-637X/779/1/52](https://doi.org/10.1088/0004-637X/779/1/52)
- Kacprzak, G. G., Muzahid, S., Churchill, C. W., Nielsen, N. M., & Charlton, J. C. 2015, ApJ, 815, 22, doi: [10.1088/0004-637X/815/1/22](https://doi.org/10.1088/0004-637X/815/1/22)
- Karman, W., Caputi, K. I., Caminha, G. B., et al. 2017, A&A, 599, A28, doi: [10.1051/0004-6361/201629055](https://doi.org/10.1051/0004-6361/201629055)
- Kornei, K. A., Shapley, A. E., Martin, C. L., et al. 2012, ApJ, 758, 135, doi: [10.1088/0004-637X/758/2/135](https://doi.org/10.1088/0004-637X/758/2/135)
- Leethochawalit, N., Jones, T. A., Ellis, R. S., Stark, D. P., & Zitrin, A. 2016, ApJ, 831, 152, doi: [10.3847/0004-637X/831/2/152](https://doi.org/10.3847/0004-637X/831/2/152)
- Manzano-King, C. M., Canalizo, G., & Sales, L. V. 2019, ApJ, 884, 54, doi: [10.3847/1538-4357/ab4197](https://doi.org/10.3847/1538-4357/ab4197)
- Markwardt, C. B. 2009, in Astronomical Society of the Pacific Conference Series, Vol. 411, Astronomical Data Analysis Software and Systems XVIII, ed. D. A. Bohlender, D. Durand, & P. Dowler, 251
- Marrone, D. P., Spilker, J. S., Hayward, C. C., et al. 2018, Nature, 553, 51, doi: [10.1038/nature24629](https://doi.org/10.1038/nature24629)
- Martin, C. L. 2005, ApJ, 621, 227, doi: [10.1086/427277](https://doi.org/10.1086/427277)
- Martin, C. L., Shapley, A. E., Coil, A. L., et al. 2012, ApJ, 760, 127, doi: [10.1088/0004-637X/760/2/127](https://doi.org/10.1088/0004-637X/760/2/127)
- Mitchell, P. D., Blaizot, J., Devriendt, J., et al. 2018, MNRAS, 474, 4279, doi: [10.1093/mnras/stx3017](https://doi.org/10.1093/mnras/stx3017)
- Mo, H. J., & White, S. D. M. 2002, MNRAS, 336, 112, doi: [10.1046/j.1365-8711.2002.05723.x](https://doi.org/10.1046/j.1365-8711.2002.05723.x)
- Muratov, A. L., Kereš, D., Faucher-Giguère, C.-A., et al. 2015, MNRAS, 454, 2691, doi: [10.1093/mnras/stv2126](https://doi.org/10.1093/mnras/stv2126)
- Muzahid, S., Kacprzak, G. G., Churchill, C. W., et al. 2015, ApJ, 811, 132, doi: [10.1088/0004-637X/811/2/132](https://doi.org/10.1088/0004-637X/811/2/132)
- Nelson, D., Pillepich, A., Springel, V., et al. 2019, MNRAS, 2010, doi: [10.1093/mnras/stz2306](https://doi.org/10.1093/mnras/stz2306)

- Newman, J. A., Cooper, M. C., Davis, M., et al. 2013, *ApJS*, 208, 5, doi: [10.1088/0067-0049/208/1/5](https://doi.org/10.1088/0067-0049/208/1/5)
- Oppenheimer, B. D., Davé, R., Kereš, D., et al. 2010, *MNRAS*, 406, 2325, doi: [10.1111/j.1365-2966.2010.16872.x](https://doi.org/10.1111/j.1365-2966.2010.16872.x)
- Pavesi, R., Riechers, D. A., Capak, P. L., et al. 2016, *ApJ*, 832, 151, doi: [10.3847/0004-637X/832/2/151](https://doi.org/10.3847/0004-637X/832/2/151)
- Penny, S. J., Masters, K. L., Smethurst, R., et al. 2018, *MNRAS*, 476, 979, doi: [10.1093/mnras/sty202](https://doi.org/10.1093/mnras/sty202)
- Reddy, N. A., Steidel, C. C., Pettini, M., et al. 2008, *ApJS*, 175, 48, doi: [10.1086/521105](https://doi.org/10.1086/521105)
- Roberts-Borsani, G. W., & Saintonge, A. 2019, *MNRAS*, 482, 4111, doi: [10.1093/mnras/sty2824](https://doi.org/10.1093/mnras/sty2824)
- Robertson, B. E., Ellis, R. S., Furlanetto, S. R., & Dunlop, J. S. 2015, *ApJL*, 802, L19, doi: [10.1088/2041-8205/802/2/L19](https://doi.org/10.1088/2041-8205/802/2/L19)
- Rubin, K. H. R., Prochaska, J. X., Koo, D. C., et al. 2014, *ApJ*, 794, 156, doi: [10.1088/0004-637X/794/2/156](https://doi.org/10.1088/0004-637X/794/2/156)
- Rupke, D. S., Veilleux, S., & Sanders, D. B. 2005a, *ApJS*, 160, 87, doi: [10.1086/432886](https://doi.org/10.1086/432886)
- . 2005b, *ApJS*, 160, 115, doi: [10.1086/432889](https://doi.org/10.1086/432889)
- Schroetter, I., Bouché, N., Péroux, C., et al. 2015, *ApJ*, 804, 83, doi: [10.1088/0004-637X/804/2/83](https://doi.org/10.1088/0004-637X/804/2/83)
- Schroetter, I., Bouché, N., Wendt, M., et al. 2016, *ApJ*, 833, 39, doi: [10.3847/1538-4357/833/1/39](https://doi.org/10.3847/1538-4357/833/1/39)
- Scoville, N., Aussel, H., Brusa, M., et al. 2007, *ApJS*, 172, 1, doi: [10.1086/516585](https://doi.org/10.1086/516585)
- Shapley, A. E., Steidel, C. C., Pettini, M., & Adelberger, K. L. 2003, *ApJ*, 588, 65, doi: [10.1086/373922](https://doi.org/10.1086/373922)
- Sharma, M., Theuns, T., Frenk, C., et al. 2017, *MNRAS*, 468, 2176, doi: [10.1093/mnras/stx578](https://doi.org/10.1093/mnras/stx578)
- Shibuya, T., Ouchi, M., & Harikane, Y. 2015, *ApJS*, 219, 15, doi: [10.1088/0067-0049/219/2/15](https://doi.org/10.1088/0067-0049/219/2/15)
- Shibuya, T., Ouchi, M., Nakajima, K., et al. 2014, *ApJ*, 788, 74, doi: [10.1088/0004-637X/788/1/74](https://doi.org/10.1088/0004-637X/788/1/74)
- Somerville, R. S., & Davé, R. 2015, *ARA&A*, 53, 51, doi: [10.1146/annurev-astro-082812-140951](https://doi.org/10.1146/annurev-astro-082812-140951)
- Speagle, J. S., Steinhardt, C. L., Capak, P. L., & Silverman, J. D. 2014, *ApJS*, 214, 15, doi: [10.1088/0067-0049/214/2/15](https://doi.org/10.1088/0067-0049/214/2/15)
- Steidel, C. C., Adelberger, K. L., Shapley, A. E., et al. 2003, *ApJ*, 592, 728, doi: [10.1086/375772](https://doi.org/10.1086/375772)
- Steidel, C. C., Erb, D. K., Shapley, A. E., et al. 2010, *ApJ*, 717, 289, doi: [10.1088/0004-637X/717/1/289](https://doi.org/10.1088/0004-637X/717/1/289)
- Steidel, C. C., Shapley, A. E., Pettini, M., et al. 2004, *ApJ*, 604, 534, doi: [10.1086/381960](https://doi.org/10.1086/381960)
- Steinhardt, C. L., Speagle, J. S., Capak, P., et al. 2014, *ApJL*, 791, L25, doi: [10.1088/2041-8205/791/2/L25](https://doi.org/10.1088/2041-8205/791/2/L25)
- Sugahara, Y., Ouchi, M., Lin, L., et al. 2017, *ApJ*, 850, 51, doi: [10.3847/1538-4357/aa956d](https://doi.org/10.3847/1538-4357/aa956d)
- Swinbank, M., Harrison, C., Tiley, A., et al. 2019, arXiv e-prints. <https://arxiv.org/abs/1906.05311>
- Tacchella, S., Bose, S., Conroy, C., Eisenstein, D. J., & Johnson, B. D. 2018, *ApJ*, 868, 92, doi: [10.3847/1538-4357/aae8e0](https://doi.org/10.3847/1538-4357/aae8e0)
- Trainor, R. F., Steidel, C. C., Strom, A. L., & Rudie, G. C. 2015, *ApJ*, 809, 89, doi: [10.1088/0004-637X/809/1/89](https://doi.org/10.1088/0004-637X/809/1/89)
- Veilleux, S., Cecil, G., & Bland-Hawthorn, J. 2005, *ARA&A*, 43, 769, doi: [10.1146/annurev.astro.43.072103.150610](https://doi.org/10.1146/annurev.astro.43.072103.150610)
- Walter, F., Riechers, D., Novak, M., et al. 2018, *ApJL*, 869, L22, doi: [10.3847/2041-8213/aaf4fa](https://doi.org/10.3847/2041-8213/aaf4fa)
- Weiner, B. J., Coil, A. L., Prochaska, J. X., et al. 2009, *ApJ*, 692, 187, doi: [10.1088/0004-637X/692/1/187](https://doi.org/10.1088/0004-637X/692/1/187)
- Zhu, G. B., Comparat, J., Kneib, J.-P., et al. 2015, *ApJ*, 815, 48, doi: [10.1088/0004-637X/815/1/48](https://doi.org/10.1088/0004-637X/815/1/48)